

Experimental study on the effect of an artificial cardiac valve on the left ventricular flow

JiangSheng Wang¹ · Qi Gao¹  · RunJie Wei² · JinJun Wang¹

Received: 30 September 2016 / Revised: 4 August 2017 / Accepted: 6 August 2017 / Published online: 29 August 2017
© Springer-Verlag GmbH Germany 2017

Abstract The use of artificial valves to replace diseased human heart valves is currently the main solution to address the malfunctioning of these valves. However, the effect of artificial valves on the ventricular flow still needs to be understood in flow physics. The left ventricular flow downstream of a St. Jude Medical (SJM) bileaflet mechanical heart valve (BMHV), which is a widely implanted mechanical bileaflet valve, is investigated with time-resolved particle image velocimetry in the current work. A tilting-disk valve is installed on the aortic orifice to guarantee unidirectional flow. Several post-processing tools are applied to provide combined analyses of the physics involved in the ventricular flow. The triple jet pattern that is closely related to the characteristics of the bileaflet valve is discussed in detail from both Eulerian and Lagrangian views. The effects of large-scale vortices on the transportation of blood are revealed by the combined analysis of the tracking of Lagrangian coherent structures, the Eulerian monitoring of the shear stresses, and virtual dye visualization. It is found that the utilization of the SJM BMHV complicates the ventricular flow and could reduce the efficiency of blood transportation. In addition, the kinematics of the bileaflets is presented to explore the effects of flow structures on their motion. These combined analyses could elucidate the properties of SJM BMHV. Furthermore, they could provide new insights into the understanding of other complex blood flows.

1 Introduction

In the past few years, an increasing number of artificial cardiac valve replacement surgeries have been performed to cure a few types of heart valve diseases. However, all mechanical heart valve replacements are plagued by complications associated with hemolysis and thrombo-embolism (Gott et al. 2003; Yoganathan et al. 2004; Dasi et al. 2009; Pibarot and Dumesnil 2009). Lifelong anticoagulation therapy, which causes considerable pain for patients, is necessary to remit these complications (Gott et al. 2003; Pibarot and Dumesnil 2009). Therefore, it is important to understand the non-physiological phenomena underlying valve implantation in physics (Kaminsky et al. 2008; Dasi et al. 2009). To date, the triple jet pattern (Kaminsky et al. 2008; Querzoli et al. 2010), large-scale vortex structures (Pierrakos et al. 2004; Pierrakos and Vlachos 2006; Querzoli et al. 2010), and inverse flow (Yoganathan et al. 2004; Le and Sotiropoulos 2013; Sotiropoulos et al. 2016) are typical flow phenomena that emanate from the replacement of mechanical bileaflet valves. The comprehension of these typical flow phenomena could be a good start for understanding the complex non-physiological ventricular flow resulting from the implantation of mechanical bileaflet valves.

Experimental measurements in ventricular flow have made significant progress both in vivo and in vitro. Great improvements of medical techniques, such as echocardiography (Hendabadi et al. 2013; Bermejo et al. 2015; Pedrizzetti and Domenichini 2015) and magnetic resonance imaging (Eriksson et al. 2011, 2012; Toger et al. 2012; Bermejo et al. 2015), permit more information on the in vivo blood flow to be revealed in detail. However, ensuring the repeatability of these experiments on unique in vivo blood flows is difficult, and this adversely impacts the understanding of the general physics of the phenomena. On the other hand, an

✉ Qi Gao
qigao@buaa.edu.cn

¹ Key Laboratory of Fluid Mechanics, Ministry of Education, Beijing University of Aeronautics and Astronautics, Beijing 100191, China

² MicroVec., Inc, Beijing 100083, China

experimental study combined with particle image velocimetry (PIV) can furnish a more satisfying in vitro dataset in terms of accuracy and reproducibility (Pierrakos et al. 2004; Cenedese et al. 2005; Akutsu and Saito 2006). After applying efficient post-processing techniques, the PIV data can be expected to provide abundant information. Obviously, PIV, with its advantages in terms of the measurement of fluid mechanics, appeals to an increasing number of applications for the assessment of prosthetic heart devices. Indeed, a new technique combining echocardiography with PIV has shown potential in the measurement of ventricular flow (Faludi et al. 2010; Kheradvar et al. 2010). The application of in vitro PIV measurements necessitates the use of a well-designed model of the left ventricle. Flexible ventricle models that are mostly produced from silicon rubber have shown potential in physiological simulations of the left ventricle (Cenedese et al. 2005; Kheradvar and Gharib 2009; Kheradvar and Falahatpisheh 2012; Fortini et al. 2014; Badas et al. 2015; Tan et al. 2016). This type of flexible model is also adopted in the current investigation.

As a typical flow structure, the triple jet pattern associated with SJM BMHV has been extensively explored with pipe configurations (Dasi et al. 2007, 2009; Yun et al. 2014a, b). The results suggested that the triple jet pattern within a pipe configuration would be symmetric. As this pattern could be influenced by the ventricle wall, it is necessary to investigate this flow pattern with a ventricle configuration. Garitey et al. (1995) employed pulsed ultrasound Doppler velocimetry to investigate the ventricular flow downstream of the SJM BMHV. However, as a point-measurement technique, it is very difficult to access detailed information on the entire flow field with Doppler velocimetry. Fortini et al. (2008) conducted an investigation of the ventricular flow with a prosthetic bileaflet valve in the mitral position. The triple jet pattern associated with the bileaflet valve was captured. However, only the Sorin Bicarbon bileaflet valve was assessed, rather than the SJM BMHV. As there are discrepancies between the configuration of the Sorin Bicarbon bileaflet valve and the SJM BMHV, the triple jet pattern associated with the SJM BMHV could be different from that associated with the Sorin Bicarbon bileaflet valve according to the conclusion of Garitey et al. (1995). Okafor et al. (2015) reported a valuable in vitro investigation of the left ventricular flow downstream of the SJM BMHV. However, in their experiments, the SJM BMHV was located upstream of the mitral annulus. As a result, the triple jet pattern developed upstream of the mitral orifice and was not observed in the ventricular flow. Thus, the triple jet pattern downstream of the SJM BMHV with the ventricular configuration has not yet been investigated. This issue is the focus of the current work.

Large-scale vortices exist in the ventricle irrespective of whether the valves are natural or prosthetic. Although the

vortices in a healthy ventricle could promote blood transport and exchange (Faludi et al. 2010; Pedrizzetti et al. 2010; Toger et al. 2012), their influence and mechanics remain unclear. According to previous investigations on bileaflet valves (Dasi et al. 2007; Fortini et al. 2008; Yun et al. 2014a, b), the triple jet pattern could completely change the vortex dynamics of the left ventricular flow and this merits further exploration. Revealing the effects of large-scale vortex structures (originating from the implantation of SJM BMHV) on the transportation of blood is also a focus point of the current work.

Yoganathan et al. (2004) and Dasi et al. (2009) pointed out that the inverse flow in the inlet of the left ventricle was a critical and inevitable phenomenon during the closure of the artificial valve. In the numerical simulation of Le and Sotiropoulos (2013), the inverse flow was asymmetrical when the leaflet was closing. This asymmetry was conjectured to be ascribed to the asymmetrical movement of the leaflets. The potential interaction between this inverse flow and the leaflet of SJM BMHV is explored in the current work.

Several advanced post-processing techniques have shown the potential to facilitate a deep comprehension of the blood flow. The phase average has been utilized successfully to extract large-scale coherent structures from the turbulent ventricle flow (Cenedese et al. 2005). This tool could also benefit the current work. Oseen vortex fitting has shown potential in extracting vortex-dynamic information from the turbulent boundary layer (Carlier and Stanislas 2005), axisymmetric stagnation flow (Wang et al. 2013), and square cylinder wake flow (He et al. 2014). This vortex detection method is also expected to reveal the vortex dynamics in the left ventricular flow. As the main source of hemolysis and thrombo-embolism (Grigioni et al. 2002, 2004; Fallon et al. 2007), the shear stress can be monitored to assess the efficiency of artificial valves. Finite-time Lyapunov exponents (FTLE) can yield insight into how blood is transported by revealing the Lagrangian coherent structures (LCSs) in the blood flow (Shadden and Taylor 2008; Shadden et al. 2010). Although this technique has been used to study the left ventricular flow with natural heart valves both in vitro (Espa et al. 2012; Badas et al. 2015) and in vivo (Hendabadi et al. 2013), analyses that combine FTLE and shear stress monitoring, which could provide more information about the effect of a prosthetic valve on the transportation properties of the ventricle flow in the current work, have not been reported in the literature. Meanwhile, virtual dye visualization (VDV) has been successfully applied to depict the vortex interactions in a wake-induced bypass transition (He et al. 2017). This method is also expected to provide intuitive visualization of the blood transportation and mixing in the current work.

The present work focuses on ventricular flow with a SJM BMHV on the mitral position and a tilting-disk valve on the

aortic position. The full flow field measurement of the symmetric plane of the ventricular flow is performed with PIV. Typical flow phenomena downstream of the SJM BMHV are discussed in detail in terms of the flow physics using several post-processing tools in combination. These combined analyses could facilitate the comprehension of the flow physics of the left ventricular flow downstream of the SJM BMHV and shed new light on other complex blood flows.

2 Experimental setups and methods

2.1 Experimental setups

The experiment mainly followed the setup of Cenedese et al. (2005). Figure 1a illustrates the experimental setup used in the current work. The flexible and transparent model of the left ventricle (7 in the figure) was produced from silicone rubber. The geometry of the model was approximated as a semi-ellipsoidal shape, with minor and major radii of 33 and 66 mm, respectively. The thickness of the model was limited to ~ 1 mm to minimize refraction in the PIV experiment. Both distilled water (refractive index of 1.33) and 1,2-propanediol (refractive index of 1.43) were tested for index matching with the silicone rubber model (refractive index of 1.43). The test with 1,2-propanediol was the control experiment of the test with distilled water. It was found that the imaging distortion associated with refraction in the distilled water test was negligible. Therefore, we followed the strategy of Cenedese et al. (2005) using distilled water as the working fluid. The geometric size of the silicone model is shown

in Fig. 1b. The model was fixed to an acrylic disk that had two orifices with different sizes. According to clinical experience (Gott et al. 2003) and anatomy (Sotiropoulos et al. 2016), it is common to have a bileaflet valve mounted in the mitral position. Therefore, the SJM BMHV was mounted on the mitral orifice (MO). A tilting-disk valve was placed on the aortic orifice (AO). These two artificial cardiac valves worked concurrently to guarantee a unidirectional flow within the circulation system (Fig. 1b). Two acrylic pipes (4) connected the heart model to a tank (5) that provided a constant water head to simulate the pressure in the blood circulation system. The silicone model was immersed in a sealed acrylic chamber (8) filled with distilled water. The chamber made it possible to visualize the PIV measurements. The field of view was illuminated by a thin light sheet (thickness of ~ 1 mm) from an 8-W semiconductor continuous laser (532 nm, 3 in Fig. 1a). A high-speed CMOS camera (6) with a telephoto lens (focal length of 90 mm) was utilized for PIV measurement with high spatial and temporal resolution. The water in the chamber was driven by a piston in the pipe (2) extending from the sidewall. The piston was electronically controlled by a servomotor (1) through a special cam, which was designed according to the physiological volume change law of the left ventricle (Cenedese et al. 2005). The volume of the heart model would change following the motion of the piston.

2.2 Experimental parameters

For the PIV measurement, the sampling frequency of the CMOS camera was 250 Hz at a full resolution of $2048 \times$

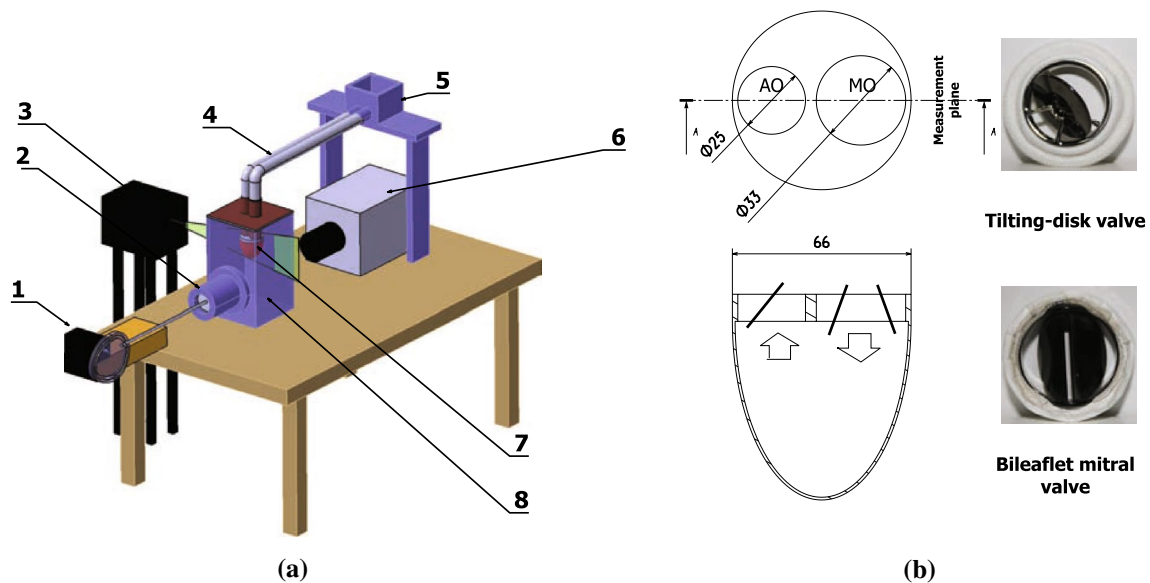


Fig. 1 a Sketch of the experimental setup. 1 Servomotor, 2 pipe with piston, 3 semiconductor continuous laser, 4 acrylic pipes, 5 water head, 6 CMOS camera, 7 ventricle model, 8 acrylic chamber; b physical model of the left ventricle

2048 pixels. The tracer particles were hollow glass beads with an average diameter of 30 μm . Both background noise reduction and image pre-processing with a Gaussian filter were utilized to improve the quality of the original images (Gao et al. 2012). The velocity vectors were calculated based on the cross-correlation algorithm between two successive images using MicroVec V3 (Microvec Inc). An algorithm similar to the window displacement iterative multigrid (WIDIM) method (Scarano 2002) was used to improve the resolution of the velocity gradients in the complex ventricular flow. The initial interrogation window size was set to be 64×64 pixels, and the final size was 32×32 pixels with an overlap of 50%. The relative uncertainty of this measurement was estimated to be less than 2%. Eventually, an outlier detection and correction technique was employed to improve the precision of the velocity field (Wang et al. 2015). Except for special definitions of local coordinate systems, the origin of the coordinate system was located in the bottom left corner of the field of view. X and Y denote the horizontal and vertical directions, respectively, and u and v represent the horizontal and vertical velocity, respectively.

The non-dimensional numbers were defined as follows:

$$\text{Reynolds number, } R_e = \frac{UD}{\nu} = 4850, \quad (1)$$

$$\text{Womersley number, } W_o = \sqrt{\frac{D^2}{Tv}} = 20.5, \quad (2)$$

where U is the peak velocity of the average flow through the mitral orifice, D is the diameter of the orifice, ν is the kinematic viscosity of distilled water, and T is the period of one beat in the current ventricle simulation. The stroke volume of the left ventricle model was fixed to approximate the physiological status. As the viscosity of blood is almost thrice that of water, T was thrice the period of the physiological cardiac cycle to correspond to the W_o and R_e . This strategy is similar to the design of Cenedese et al. (2005).

2.3 Data analysis methods

2.3.1 Phase average based on proper orthogonal decomposition (POD)

The phase average technique in the current work is an extended application based on proper orthogonal decomposition (POD) (Pan et al. 2013). The technique extracts phase information from the relation between the time coefficients of the first two POD modes. Consequently, the phase average is executed to extract the key flow patterns from the turbulent ventricular flow according to the phase information (40 cycles were used in this process).

2.3.2 Vortex tracking based on Oseen vortex fitting and the criterion of λ_{ci}

The criterion of the swirl strength λ_{ci} (Zhou et al. 1999) is utilized for differentiating between the rotation and shear motions of the flow. The Oseen vortex model with a Gaussian-like vorticity distribution (Carlier and Stanislas 2005) is employed as a template to fit the high-concentration region of λ_{ci} . Once the fitting is considered sufficient, the core position and the convection velocity of the vortex can be acquired. The algorithm was detailed by Wang et al. (2013).

2.3.3 Lagrangian coherent structures (LCSs) tracking based on the finite-time Lyapunov exponents (FTLE) method

The FTLE extracts the exponential divergence of nearby trajectories over a finite-time interval (Shadden et al. 2006). These trajectories can be integrated backward (with a negative time interval) based on the velocity field to obtain the FTLE ridges with attracting properties. These ridges can be treated as Lagrangian coherent structures (LCSs). In the current work, the time interval for this backward integration equals T . Shadden et al. (2005) proved that the flux of particles through the ridge of FTLE was indeed negligible. Therefore, the enclosing ridges can outline the boundary of a flow region that has no material exchange with nearby fluid. The effect of large-scale vortices on the transportation of blood in the left ventricle could be assessed based on this characteristic.

2.3.4 Virtual dye visualization (VDV)

Synthetic particle tracking has been utilized to reveal the Lagrangian dynamic of the healthy left ventricular flow (Espa et al. 2012; Badas et al. 2015). After describing the brightness of the synthetic particles following a Gaussian intensity profile (He et al. 2017), the cluster of the virtual tracer particles can mimic the visualization using a real dye. Assigning different colors to the synthetic particles makes it possible to visualize different flow structures more intuitively. In the current work, the blood transportation is also visualized by VDV. Virtual dyes in the three primary colors are respectively released near the three orifices of the SJM BMHV. Consequently, according to the different colors, the blood in the ventricle can be easily traced to the different jets of the triple jet pattern. The mixing of blood and the three-dimensional flow out of the measurement plane can also be determined by observing the mixing colors of the virtual dyes.

3 Results and discussions

It should be emphasized that all the data analyses in the current work are based on the six characteristic phases of one cardiac cycle, as suggested by Cenedese et al. (2005). These phases are indicated by the red points in Fig. 2. The details of the phases are:

- (a) Peak of the early diastolic wave (E wave);
- (b) End of the E wave;
- (c) Peak of the secondary diastolic wave (A wave);
- (d) End of the A wave;
- (e) Peak of the systole;
- (f) End of the systole.

3.1 Validation of the experimental model

In a left ventricle simulator, the real volume variation of the ventricle model is required to satisfy the physiological volume change law. Fortini et al. (2013) utilized the flow rates at the inlet and outlet to represent the variation in the ventricle volume. They found that the flow rate calculated from the velocity matched the flow rate calculated from the physiological volume variation law. In the current work, the actual ventricle volume is calculated directly from the PIV raw image. Since the volume of the left ventricle is a parameter that is used directly in the physiological law, it is considered to be an intuitional parameter to validate the experimental model. This approach is detailed in Fig. 3. The volume variation of the left ventricle model in one cardiac cycle is provided in Fig. 5 as a red curve. The high correlation coefficient (equal to 0.974) between the

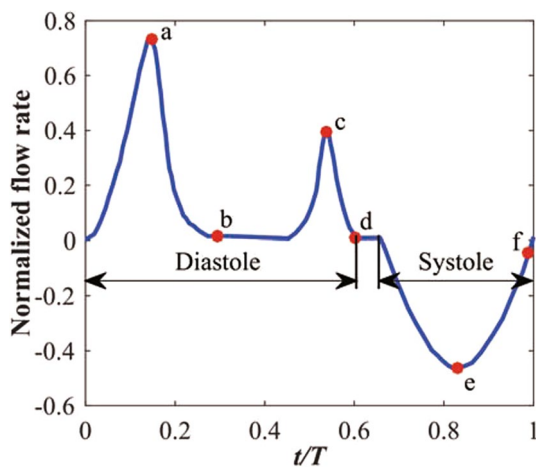


Fig. 2 Normalized flow rate as a function of time (Cenedese et al. 2005). The red points represent the six characteristic instants in one cardiac cycle

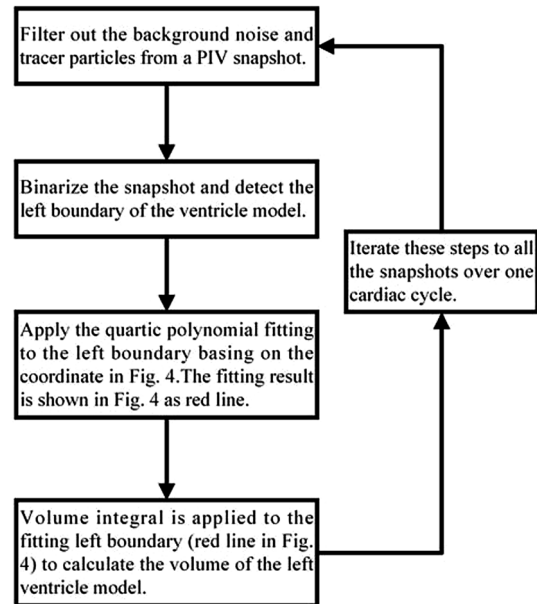


Fig. 3 Procedures for acquiring the volume variation of the left ventricle model

experimental simulation curve and the theoretical curve (black line in Fig. 5) suggests good agreement between the experimental simulation and the physiological status (Fig. 4).

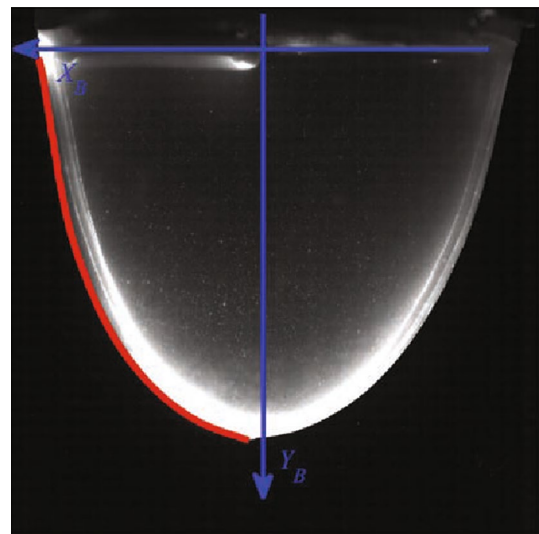


Fig. 4 Sketch of the left ventricle model. The red curve represents the left boundary of the model. The local y-coordinate (Y_B) is defined along the central symmetry axis of the ventricle model. The local x-coordinate (X_B) is defined along the bottom surface of the acrylic disk

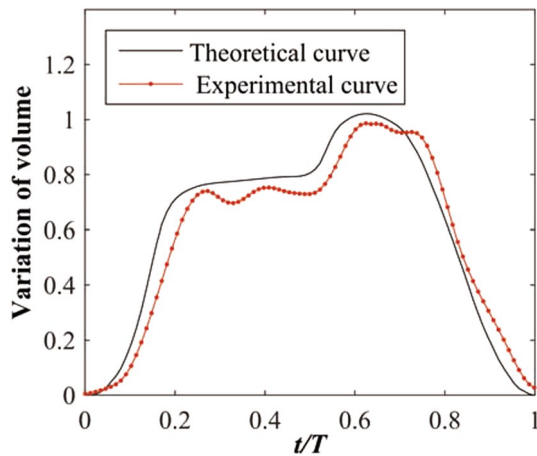


Fig. 5 Normalized volume variations of the left ventricle model in physiology (*black curve*) and in experimental simulation (*red curve*). The physiological curve is obtained from Cenedese et al. (2005)

3.2 Triple jet pattern

The two leaflets of the bileaflet mechanical heart valve split the annular housing into three orifices. The blood flow through these three orifices is divided into three jets. These three jets combined with the vortices generated from them are known as the triple jet pattern following the definition of Yoganathan et al. (2004). In this section, the triple jet pattern downstream of the SJM BMHV within the left ventricular flow is discussed based on the vorticity contours. The shear stress associated with the triple jet pattern is assessed since it might be highly related to the damage inflicted upon blood cells (Grigioni et al. 2002, 2004; Cenedese et al. 2005; Fallon et al. 2007). The results of vortex tracking supplement the detailed dynamic information of the two large-scale vortices originating from the triple jet pattern.

3.2.1 Vorticity

The vorticity contours of the six characteristic phases are given in Fig. 6. Two jet-like structures are generated from the two lateral orifices in Fig. 6a. As implied by Yun et al. (2014a), a retrograde jet could be formed in the narrow gap between the two leaflets due to their rapid opening. In Fig. 6a, the delayed emergence of the jet-like structure in the middle gap (confined by the two leaflets) might be attributed to this retrograde jet. Meanwhile, the narrow middle gap also results in more stagnation than in the two broad lateral passageways. This discrepancy of stagnation may also contribute to the delayed emergence of the middle jet-like structure. The interactions between these two lateral jets result in only two large-scale vortices (this is confirmed by the vortex tracking), which are labeled as the left (L) and right (R) vortices. The position of R is vertically lower than that

of L. Three potential causes could contribute to the deviation between the positions of L and R:

- During the opening cycle, the right leaflet moves faster than the left one (further discussed in Sect. 3.4) resulting in a stronger jet in the right passageway than in the left one;
- The right boundary of the model provides a contractive geometry to accelerate the right jet;
- The upward mean flow in the left half of the ventricle (as shown in Fig. 7) could impede the development of the left jet.

All these reasons could contribute to a higher velocity in the right passageway than in the left one (Fig. 7) and a subsequent faster convection of R than of L.

At the end of the E wave (Fig. 6b), the two vortices become detached from the free shear layer of the jet-like structures since there is no longer a continuous momentum input from the inlet flow. The middle jet appears at this instant. Consequently, a triple jet pattern is formed. This flow pattern is similar to the numerical results of Choi et al. (2014). The similar ventricle model with a similar bileaflet mechanical valve could contribute to this similar flow pattern. In this snapshot, the deviation of the vertical position between the two vortices is more evident. As mentioned previously, the right vortex (R) is stronger and moves faster than the left vortex (L). Therefore, the deviation between the vertical positions of these two vortices could expose L to an additional upward retardation from the induction of R. Eventually, the retardation from both the right vortex induction and the upward mean flow on the left half of the ventricle stabilize the left vortex in the middle region of the ventricle.

In comparison with the triple jet pattern downstream of the Sorin Bicarbon bileaflet valve with a left ventricular configuration (Fortini et al. 2008; Querzoli et al. 2010), a few discrepancies should be noted. These discrepancies could furnish additional evidence for the conclusion made by Garitey et al. (1995) that small differences in the design of artificial valves could produce a significant difference in the flow pattern of the left ventricle. For the SJM BMHV in the current work, the middle passageway is narrower than the two lateral passageways, which results in stronger stagnation in the middle passageway. Finally, the triple jet pattern contains two strong lateral jets and one weak middle jet. The interactions among these three jets only generate two large-scale vortices (L and R). Except for L and R in Fig. 6b, the remaining vorticity is the consequence of pure shear. For the Sorin Bicarbon bileaflet valve used by Querzoli et al. (2010) and Fortini et al. (2008), the three passageways are nearly equal in area when the valve is opened completely. These three equal passageways could reduce the stagnation in the middle passageway and distribute the energy of the inlet

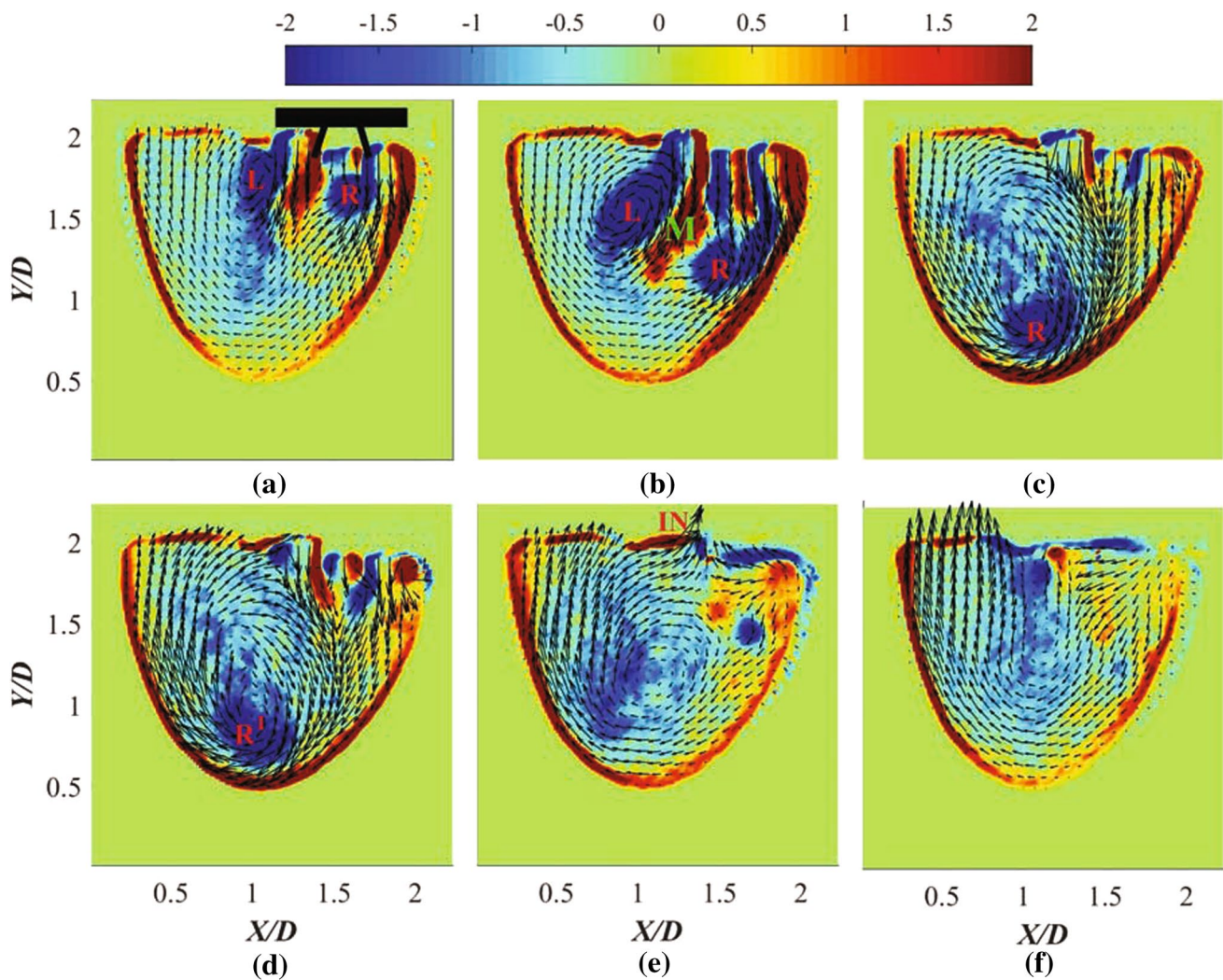


Fig. 6 Vorticity contour at characteristic instants of a cardiac cycle. **a** Peak of the E wave; **b** end of the E wave; **c** peak of the A wave; **d** end of the A wave; **e** peak of the systole; **f** near the end of the systole. The black patterning is a sketch of SJM BMHV. The clockwise vorticity is

defined as a negative value. The vorticity is rendered dimensionless by multiplying by D/U . The velocity vectors are superimposed on the vorticity contour

flow to these three jets evenly. Due to this discrepancy in the design based on the SJM BMHV, the three jets downstream of the Sorin Bicarbon bileaflet valve may be nearly equal in strength (Fortini et al. 2008). Another important difference between the current investigation and those reported in the literatures should be highlighted. In the numerical simulation by Choi et al. (2014), the mitral orifice is not directly attached and is tangent to the right wall of the ventricle. Thus, there is sufficient space to generate a counterclockwise vortex on the right side of the incoming jet (triple jet pattern). In the work of Querzoli et al. (2010), this counterclockwise vortex occurs in the case with uniform inflow (single jet pattern) and disappears in the case of the Sorin Bicarbon bileaflet valve in the mitral orifice (triple jet pattern). For a uniform inflow, although the tangent position

between the mitral orifice and the right wall of the ventricle limits the space on the right side of the incoming jet, the right shear layer of the single jet pattern can still share half of the mitral orifice to acquire sufficient space to form the counterclockwise vortex on the right side of the incoming jet. In the case of the Sorin Bicarbon bileaflet valve in the mitral orifice, the existence of the triple jet pattern causes the jet on the right to share less than half of the mitral orifice. Both the tangent position between the mitral orifice and the right wall of the ventricle and the existence of the triple jet pattern prohibit the occurrence of the counterclockwise vortex on the right side of the incoming jet. In the current work, for reasons similar to the second case of Querzoli et al. (2010), the counterclockwise vortex is also missing on the right side of the incoming jet. Thus, it is found that sufficient

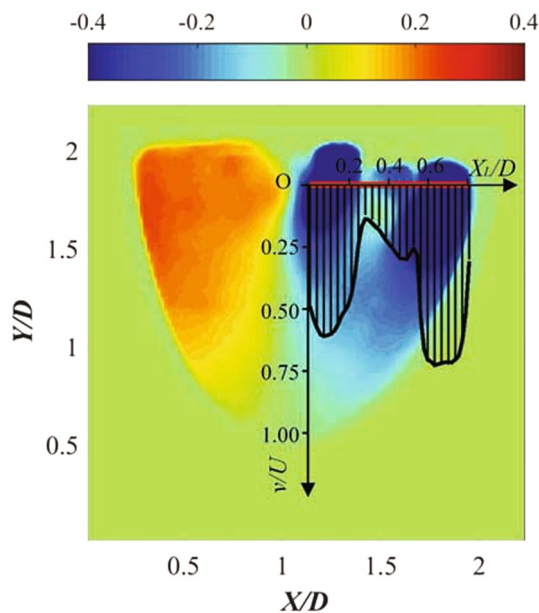


Fig. 7 Vertical velocity profile near the mitral position at the peak of the E wave. The vertical component of the velocity is shown as background contour. The *red line* represents the sampling position. The coordinates are defined according to the sampling position

space next to the wall could be a necessary condition for the formation of the counterclockwise vortex on the right side of the incoming jet.

During the A wave, a secondary triple jet-like structure, similar to the primary triple jet pattern during the E wave but with less intensity, is captured near the inlet (Fig. 6c). Induced by R in Fig. 6b, the positive vorticity (M) in the lower right corner of L is pushed toward L. Consequently, L in Fig. 6b disappears in Fig. 6c, both because of merging with the opposite vorticity (M in Fig. 6b) and because of viscous dissipation. On the other hand, R remains distinguishable in the vorticity field and is almost stable in the apex. According to the *in vivo* investigation (Son et al. 2012), the R in the apex could prevent blood-stagnation and reduce the risk of thrombus formation near the apex. In combination with the long lifetime of R, the apex is speculated to be a region suitable for persistence of the clockwise vortex, probably due to the continuous momentum supplement from the clockwise main flow in the left ventricle. At the end of the A wave (Fig. 6d), the volume of the left ventricle reaches its maximum in the whole cardiac cycle. Owing to the short period of the A wave, there is insufficient energy and time for the new jet-like structures originating from the A wave to generate a large-scale vortex.

In Fig. 6e, an inverse flow (positive vorticity IN) near the bileaflet valve can be observed. In combination with the CFD simulation results (Le and Sotiropoulos 2013; Yun et al. 2014a) and the experimental measurements (Dasi et al. 2007) on bileaflet valves, it can be concluded that the inverse

flow near the inlet of the left ventricle is an inevitable phenomenon resulting from the application of artificial bileaflet valves. Although the retrograde flow is the energy source for the closure of the bileaflet valve, a high vorticity region associated with the inverse flow indicates potential damage to blood cells, which could lead to many pathologic complications. In Fig. 6f, almost all structures in the left ventricle dissipate owing to the viscosity. Hence, one cardiac cycle is independent of other cycles with respect to vorticity. In other words, the flow evolution in one cycle is not influenced by the preceding cycle.

3.2.2 Shear stresses

Monitoring of the shear stress in the full flow field (Cenedese et al. 2005) revealed that high-shear-stress regions emerge near the inlet of the left ventricle during the diastole and near the outlet of the left ventricle during the systole. The evolution of the high-shear-stress regions observed in the current work near the ventricle wall, along with the motion of flow structures, is also described in this subsection.

At the peak of the E wave (Fig. 8a), high-shear-stress regions are observed near both the orifice of the mitral position and the boundaries of the two lateral jets. The area of the high-shear-stress regions increases along with the evolution of the triple jet pattern until the end of the E wave (Fig. 8b). Compared with the low-shear-stress distribution in the physiological health ventricle simulation (Querzoli et al. 2010), the appearance of these high-shear-stress regions is mainly attributed to the high-velocity gradients near the boundaries of the triple jet pattern. Following the definition of shear stress in Cenedese et al. (2005), the high-shear-stress regions near the ventricle wall could reflect the viscous interaction between flow structures and the wall. Due to the induction of the jet on the right, a new high-shear-stress region emerges near the right side of the ventricle wall (Fig. 8b).

During the A wave, the secondary triple jet pattern with less intensity generates a new high-shear-stress region at the inlet (Fig. 8c). This high-shear-stress region almost disappears at the end of the A wave (Fig. 8d). In addition, the high-shear-stress region near the wall moves along with the evolution of flow structures from the cardiac apex (Fig. 8c) to the top left of the apex (Fig. 8d). As indicated in Fig. 6c, R is almost stable on the apex near this instant. Compared with the high-shear-stress region near the right (Fig. 8b) and left (Fig. 8d) walls of the ventricle, the low-shear-stress values near the apex wall (Fig. 8c) indicate weak interaction between R and the apex wall in Fig. 6c.

In Fig. 8e, a high-shear-stress region related to the retrograde flow is observed near the MO. The shear stress contour is more intuitive for depicting the harm of the retrograde flow than the vorticity contour. Meanwhile, the outward flow in the left part of the ventricle induces a high-shear-stress

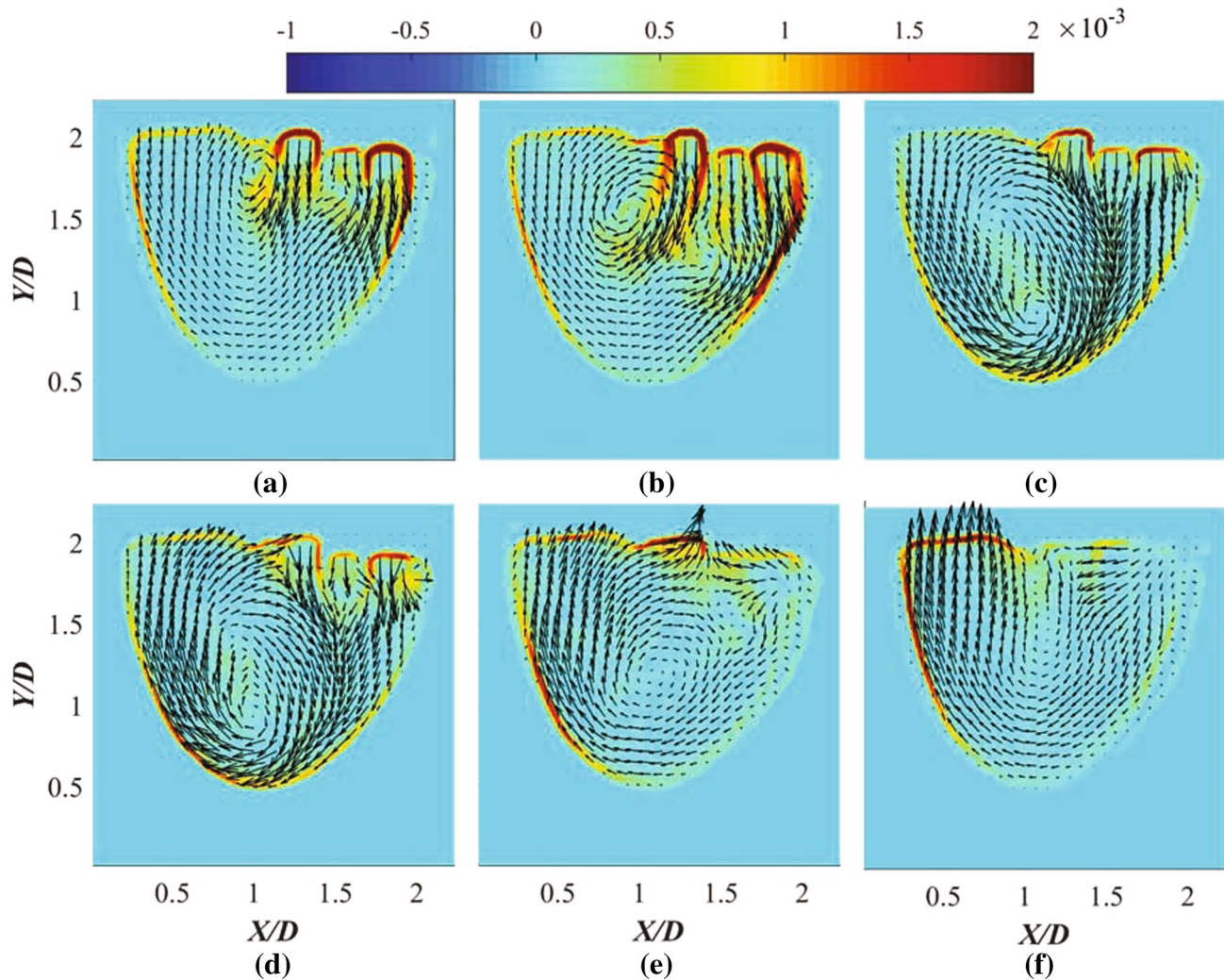


Fig. 8 Shear stress contour at characteristic instants of the cardiac cycle. **a** Peak of the E wave; **b** end of the E wave; **c** peak of the A wave; **d** end of the A wave; **e** peak of the systole; **f** near the end of the

systole. The shear stress is made dimensionless by multiplying with $1/\rho U^2$. The velocity vectors are superimposed on the shear stress contour

region near the left wall of the ventricle, and this area moves toward the aortic orifice due to the growth of the outward jet (Fig. 8f).

The shear stress contour combined with the vorticity contour in Sect. 3.2.1 and the FTLE field in Sect. 3.3 could provide additional hemodynamic information on the left ventricle flow.

3.2.3 Vortex tracking

Several previous studies have pointed out that the characteristics of the vortices in a triple jet pattern could be affected by the geometry of the left ventricle (Pierrakos et al. 2004; Cenedese et al. 2005). This deduction can be proven from the vortex tracking experiments on L and R described in this subsection. The detailed dynamic information of L and

R based on vortex tracking could provide additional evidence to facilitate comprehension of the physical aspects in Sect. 3.2.1.

The vortex core trajectories of L and R are shown in Fig. 9. The vortex cores are defined as the centers of the Oseen vortex model (Carlier and Stanislas 2005; Wang et al. 2013). The smoothing Spline in the “cftool” of MATLAB is utilized to fit the raw trajectory. The two vortices have similar paths parallel to the ventricle wall. A mechanism is proposed to generalize this phenomenon. In Fig. 9, both upper parts of the two trajectories are parallel with the upper part of the right wall of the ventricle. This phenomenon indicates that the right wall could guide the inlet jet to be bottom-left-inclined. The right vortex will move toward the apex guided by the right wall and stabilize at the apex until nearly the end of the A wave. Meanwhile, this vortex could also contribute

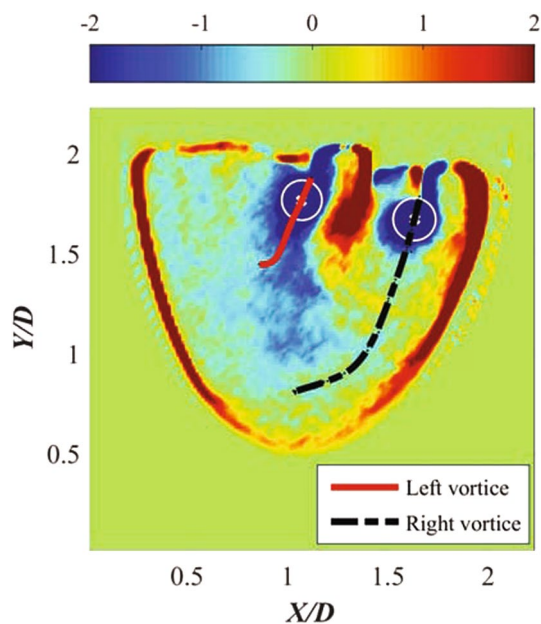


Fig. 9 Trajectories of vortex cores. The red and black curves represent the trajectories of the vortices on the left and right, respectively. The vorticity contour in Fig. 6a is also shown as the background. The final fitting of the Oseen vortex at this instant is depicted by the white circle

to a portion of the vorticity at the right wall boundary. As mentioned in Sect. 3.2.1, the right vortex moves faster than the left one. The stronger induction from the right vortex combined with the retardation from the upward main flow in the left part of the ventricle prevents the left vortex from moving toward the apex. Consequently, the left vortex is retarded in the neutral ventricular position and disappears because of both vorticity merging (between L and M in Fig. 6b) and viscous dissipation, which also results in a trajectory parallel to the right ventricle wall.

Benefiting from the Oseen vortex fitting (Carlier and Stanislas 2005; Wang et al. 2013), the convection velocity of the vortex core (V_c) can also be determined (Fig. 10). Both raw velocities of the two vortices are shown as black solid dots. The smoothing Spline in the “cftool” of MATLAB is utilized to fit the raw velocity. It is evident that the right vortex moves faster than the left one in a vertical direction throughout the entire cardiac cycle (Fig. 10). The right vortex experiences an accelerating motion followed by a decelerating motion. The phase with maximal V_c is marked as the red solid point 1 on the flow rate curve. Referring to the vorticity contour, the middle jet is first identified around this phase. In other words, the middle jet is retarded before this phase. Therefore, in addition to the reasons mentioned in Sect. 3.2.1, it is speculated that the induction from R could also impede the emergence of the middle jet. The counteracting force of the retardation could also contribute to the

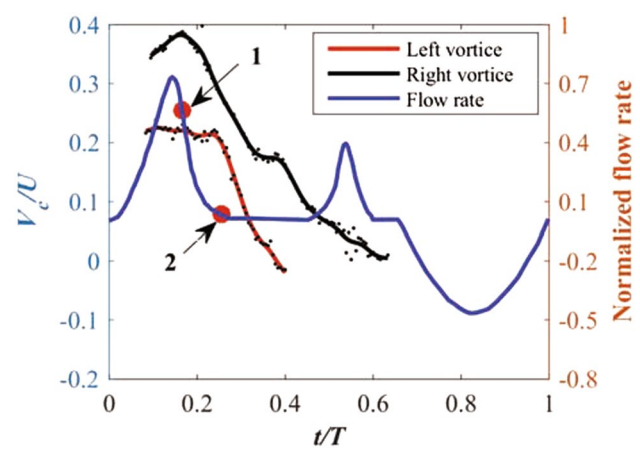


Fig. 10 Vertical convection velocity (V_c) of the vortex cores as a function of time. The red and black curves represent the V_c of the vortices on the left and the right, respectively. V_c is multiplied by -1 for intuitive display. Figure 2 is also shown as the reference curve

accelerating motion of R. For L, an almost uniform velocity is observed before the decelerating motion. The demarcation phase between these two kinds of motion is also marked on the flow rate curve as point 2 (Fig. 10). This phase is nearly located at the end of the E wave. The energy from the E wave jet, the retardation from the upward main flow in the left part of the ventricle, and the induction from the right vortex could all interact with each other to produce the uniform-velocity motion before point 2 (Fig. 10).

3.3 Effect of large-scale vortices on blood transportation

FTLE ridges with attracting properties are utilized in this part to extract LCSs. The effect of large-scale vortices on blood transportation could be revealed by tracking the evolution of LCSs (Shadden and Taylor 2008; Shadden et al. 2010; Espa et al. 2012; Hendabadi et al. 2013). The VDV is added to provide more information on the blood transportation and mixing.

3.3.1 Tracking on Lagrangian coherent structures by finite-time Lyapunov exponents

At the peak of the E wave, two jets are captured in the vorticity field (Fig. 6a) near the inlet. The same flow pattern can also be observed in the FTLE field at the same instant and position (block T_1 in Fig. 11a). Two regions with twisted ridge lines in T_1 are manifestations of the two large-scale vortices (L and R). As mentioned in Sect. 2.3.3, the flux of particles through the ridge of the FTLE is negligible. Therefore, the region with notation A_1 enclosed by the ridges has almost no fluid exchange with the neighboring flow field in

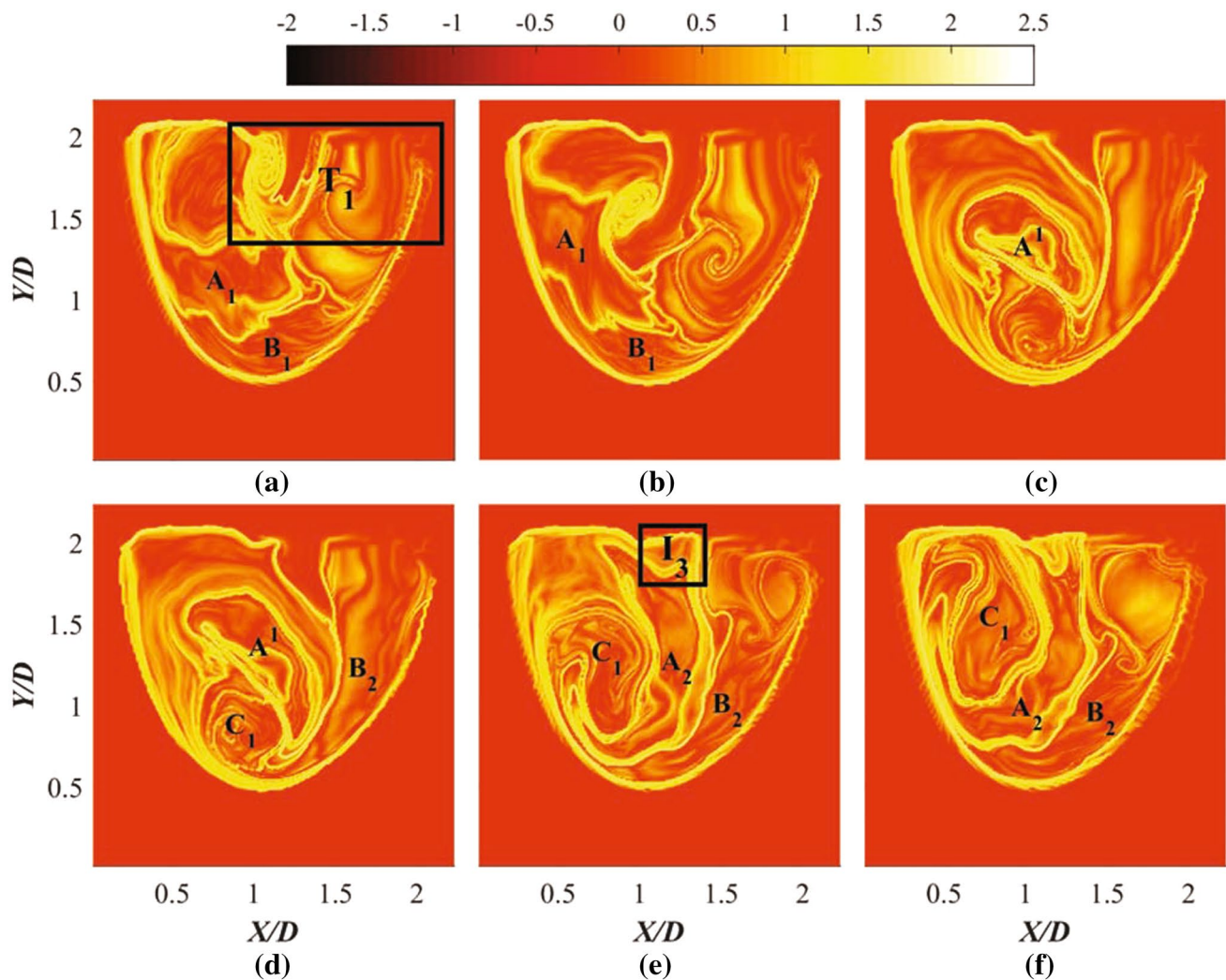


Fig. 11 FTLE fields at characteristic instants of a cardiac cycle. **a** Peak of the E wave; **b** end of the E wave; **c** peak of the A wave; **d** end of the A wave; **e** peak of the systole; **f** near the end of the systole

the measurement plane. The effect of vortex structures on A_1 reflects the effect of a vortex on blood transportation. Accordingly, the region identified by the notation B_1 has properties analogous to region A_1 . Before this phase, there are few conspicuous shape and position variations on both A_1 and B_1 . Therefore, both L and R could have few influences on the full ventricle flow. In fact, these two vortices only affect the region near the mitral position because the inlet jets are in the preliminary stage.

The vortex structures represented by the twisted ridges can still be observed in Fig. 11b. The left vortex moves to the neutral position of the left ventricle. In the Lagrangian view, it is evident that R moves faster than L in the vertical direction. Induced by L, A_1 moves upward toward the aortic position and becomes narrow in shape. Meanwhile, the aortic valve remains closed until the beginning of the systole. Consequently, no fluid is leaving the left ventricle

at this instant. The fluid in A_1 continues to remain in the ventricle during this cardiac cycle. After monitoring two cardiac cycles, a portion of the blood in A_1 could constitute a portion of the new A_1 in the next cardiac cycle. Because R is still located in the right part of the ventricle, the extent to which region A_1 is influenced by R is small. Nevertheless, R could facilitate the movement of B_1 toward the outlet.

In Fig. 11c, both A_1 and B_1 in Fig. 11b are difficult to track. The disappearance of the twisted ridges in the neutral ventricular position indicates the dissipation of L. The opposite vorticity merging between L and M in Fig. 6b is obvious before this instant because both L and M are enclosed by one ridge to merge and form region A^1 (since this region could contribute to the formation of A_1 in the next cardiac cycle, it is still denoted with the letter A). Meanwhile, the intertwined ridges that represent R remain captured in the apex of the ventricle. By monitoring other ridges near this

vortex, it is found that R continues to induce the fluid within its upper left region to move toward the outlet.

At the end of the A wave (Fig. 11d), the new region originating from the dissipated vortex at the apex is denoted as C_1 . Since the fluid in this region all originates from the jet structure at the early diastole, the fluid in C_1 can represent the fresh blood that is newly injected into the ventricle in this cardiac cycle. After tracking C_1 , it is found that one portion of the fluid in this region could depart from the ventricle through the aortic orifice during the systole and the rest could remain in the ventricle. The retained part of this region could be entrained into the vortex structure in the next cycle and constitute the new region A_1 with other fluid in the third cycle counting from the current cycle.

A retrograde flow is also observed near the mitral position in the FTLE field (I_3 in Fig. 11e). In the black box, the inverse flow can be demonstrated as a small area (enclosed by the ridges) that moves toward the inlet of the ventricle and constantly diminishes its area. It is evident that the distinct inverse flow only emerges on the left lateral passageway rather than on the other passageways. This phenomenon is further discussed in Sect. 3.4. Meanwhile, C_1 will continue moving toward the aortic valve. Two regions, which could transform to the new regions A_1 and B_1 in the next cardiac cycle, are depicted in Fig. 11e and denoted as A_2 and B_2 .

Near the end of the systole (Fig. 11f), a portion of the fluid in C_1 is prevented from leaving the ventricle owing to the closure of the aortic valve. This portion could be entrained by L in the next cardiac cycle into A_2 in the next cycle. Finally, this portion could contribute to the formation of A_1 in the third cycle counting from the current cycle. As mentioned in Sect. 3.2.1, almost all the structures in the left ventricle dissipate (due to the viscosity) at this instant, and the cardiac cycles are independent of each other from the view of the vorticity contour. However, from the viewpoint of FTLE, the flow field evolution could be influenced by the trail of the former cycle.

In summary, the existence of the triple jet pattern generated from the E wave complicates the flow structures in the left ventricle. The vortex structures that exist on the apex of the ventricle (during the A wave) could facilitate the transportation of blood toward the aortic orifice during the systole, similar to the *in vivo* situation (Faludi et al. 2010). The extent to which these complications could be attributed to the vortex originating from the left jet is larger. As discussed in Sect. 3.2.2, the triple jet pattern increases the shear stress level in the ventricle flow. A portion of fresh blood injected into the ventricle in one cycle (similar to a portion of C_1) could be adversely affected by the repeated entrainment of L in the next several cycles. The high-shear-stress region around the triple jet pattern could damage the blood cells repeatedly. Therefore, the current work indicates that the SJM BMHV could produce fearful hemodynamic

complications owing to the large-scale vortex originating from the left jet. Hence, after prosthetic valve replacement, blood cells may have a greater possibility of damage due to the accumulation of injury.

3.3.2 Virtual dye visualization

Virtual dye visualization of the third cardiac cycle (counting from the dye-emitting cycle) is shown in Fig. 12. The virtual dye with red color represents the blood originating from the left jet of the triple jet pattern (denoted as LJ). Accordingly, the green dye and the blue dye are emitted from the middle jet (MJ) and the right jet (RJ), respectively. Subscript 3 represents the blood injected during the third cardiac cycle. Subscript 2 represents the blood that is mainly injected during the second cardiac cycle.

In Fig. 12a, the blood within the ventricle mainly originates from the left and right jets. Most of the blood within LJ_2 can be traced back to the left jet of the second cardiac cycle. Two regions, both denoted as RJ_2 , mainly consist of the blood from the right jet of the second cardiac cycle. Thus, VDV can not only partition the ventricle flow into different regions but also show the origins of the blood within these regions intuitively. Furthermore, the three-dimensional flow out of the measurement plane can also be visualized by the white region representing sparsely distributed dye. However, the contiguous position between LJ_2 and LJ_3 means that this tool could fail to provide a clear material line, which can be acquired by FTLE. As the triple jet pattern evolves, a portion of the blood within MJ_3 could be entrained into R (Fig. 12b). The blood near the aortic valve (top RJ_2 in Fig. 12b) will be entrained into L. The black dye surrounding L indicates that the blood originating from the middle and right jet of the last cycle could interact with that originating from the left jet of the current cycle.

After the disappearance of L (Fig. 12c), the red dye in LJ_2 could also be entrained by the residual effect of L. The magenta dye near the mitral valve indicates mixing of the blue dye (residual blood of the top RJ_2 in Fig. 12b) and the red dye (originating from the left jet of the A wave). The white region within LJ_2 indicates the relatively strong out-of-measurement-plane flow within this region. Further, the entrained MJ_3 could mix with the bottom RJ_3 , as represented by the cyan dye around the apex. The evolution of LJ_3 could facilitate the segregation between bottom RJ_3 and top RJ_3 in Fig. 12d.

During the systole, the black dye within LJ_3 (Fig. 12e) indicates complex interaction among the blood flows originating from the different jets. The small white region around the mitral position evolves into a large white region in Fig. 12f, impelled by the three-dimensional flow around this region. At the end of the systole (Fig. 12f), the complex distribution of dye in different colors (more than three

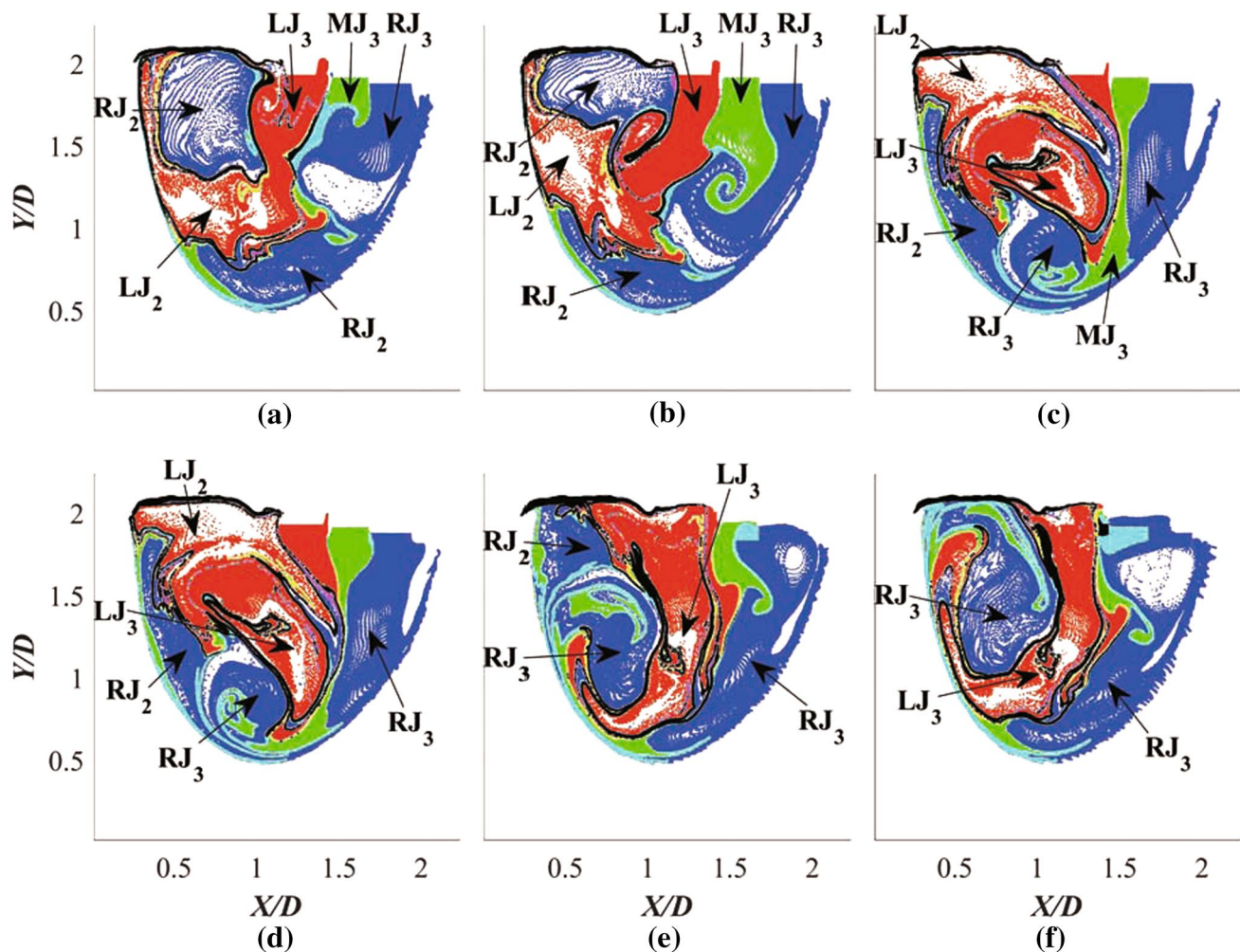


Fig. 12 Virtual dye visualization at the third cardiac cycle counting from the dye-emitting cycle. **a** Peak of the E wave; **b** end of the E wave; **c** peak of the A wave; **d** end of the A wave; **e** peak of the systole; **f** near the end of the systole

colors) reveals that the triple jet pattern causes the blood transportation and mixing to become intricate.

3.4 Inverse flow and the kinematics of the leaflets

In this section, both the asymmetric motions of the bileaflets and the retrograde flow near the bileaflet valve are discussed in detail.

3.4.1 Asymmetric kinematic properties of the leaflets

By tracking the two leaflets in the raw PIV images, it becomes possible to observe the phase deviations between the motions of the two leaflets. In Fig. 13, two characteristic instantaneous images are provided to demonstrate the asymmetric kinematic property of the leaflets. During the opening cycle, the right leaflet (R_L in Fig. 13a) moves faster than

the left one (L_L in Fig. 13a). Meanwhile, during the closing cycle, R_L closes faster than L_L .

To investigate the asymmetry quantitatively, an opening angle (θ) is defined in Fig. 13a. The two blue lines represent the bearing line of the leaflet and the horizontal line. The opening angle, which is defined as the angle between these two lines, is shown in Fig. 14 for both leaflets as a function of time. The results suggest that two phase deviations occur in one cardiac cycle. The phase lag from the left leaflet to the right leaflet is more remarkable in the closing cycle than in the opening cycle. A reasonable interpretation is provided to explain the phase deviations between the two leaflets. At the beginning of the opening cycle, a high-speed region caused by the residual effects of the outward jet in the last cardiac cycle can be observed in the left part of the ventricle. In this region, the vertical velocity points upward (similar to the red region A in Fig. 15). This high-speed region could induce a stagnation pointing toward the inlet of the ventricle. It is

Fig. 13 PIV raw images at the characteristic instants of the cardiac cycle. **a** Characteristic instant during the opening cycle; **b** characteristic instant during the closing cycle. The leaflets are highlighted by the red lines, and the direction of motion is denoted by the red arrow

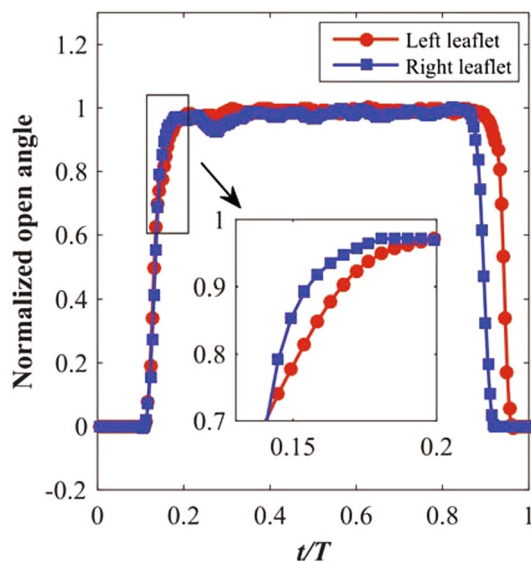
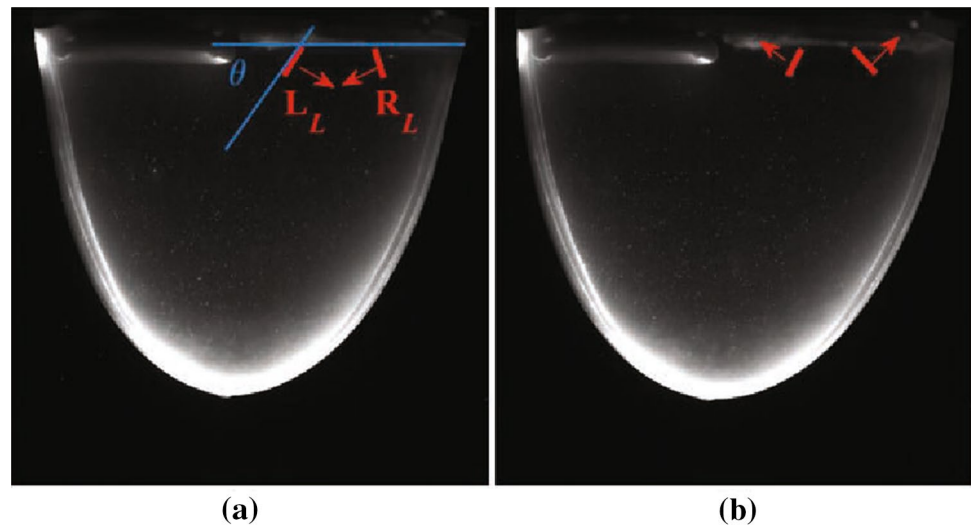


Fig. 14 Opening angle as a function of time. The red and blue lines represent the left and right leaflets, respectively. Both T and the opening angle are normalized. The insert shows an enlarged view

evident that the stagnation effect is stronger near the left leaflet than near the right leaflet, because the left leaflet is close to the high-speed region. Therefore, the left leaflet needs to overcome more resistance than the right one to be fully opened. Consequently, the right leaflet moves faster than the left one in this period.

A different mechanism could play the dominant role in the asymmetric closure. Since the bileaflet valve does not have the ability to open and close on its own, this valve is opened at the initial stage of the systole and allows a small amount of fluid to pass through it to generate a retrograde flow to provide the energy for closure. The predecessor of the retrograde flow associated with the left leaflet is marked

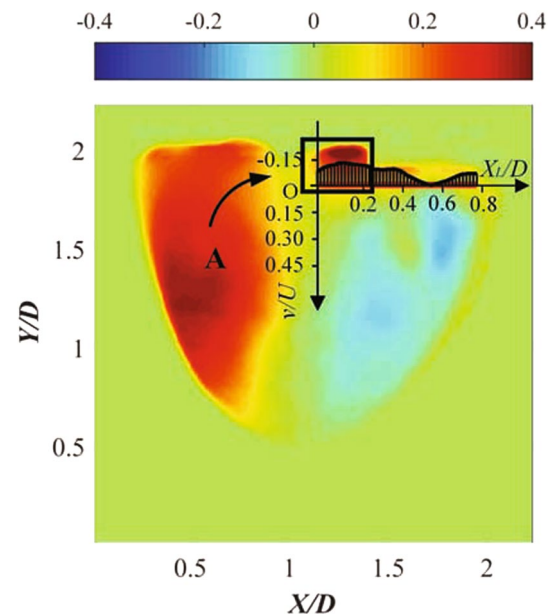


Fig. 15 Vertical velocity profile on the mitral position at the peak of the systole. The red line represents the sampling position. The coordinates are the same as those in Fig. 7. The vertical component of the velocity is shown as background contour

as a curved flow after the generalization of a number of velocity vectors (black arrow in Fig. 15). Although the retrograde flow associated with the right leaflet originates from a similar curved flow, the left curved flow is stronger and more durable than the right one, because the left one gains continuous momentum input from the outward jet. Consequently, the right retrograde flow vanishes earlier than that on the left. It is worth noting that the horizontal component of the left curved flow (black arrow in Fig. 15) could strike the left leaflet and restrain the closing motion. This

horizontal component is intensified by the tilting-disk valve in the aortic orifice with the installed orientation shown in Fig. 1b. Eventually, the stagnation of the left curved flow (black arrow in Fig. 15) is sufficiently strong to delay the closing of the left leaflet.

In addition, another possible factor needs to be considered here. Manufactured uncertainties could lead to an inherent asymmetric discrepancy between the two leaflets, such as a different drag between the two hinges and a different surface area between the two leaflets. Since these manufactured uncertainties could be small under the expectation of symmetric products, they can be neglected, in contrast with the dominant fluid mechanic factors proposed in the current work.

3.4.2 Inverse flow

As mentioned in Sect. 3.2.1, the retrograde flow is an essential flow structure in the application of bileaflet valves. This flow phenomenon is captured in the vorticity contour (Fig. 6e), shear stress contour (Fig. 8e), backward integral FTLE field (Fig. 11e), and the velocity profile near the bileaflet valve (Fig. 15). As the power source of the leaflets closure, the retrograde flow generates high shear stress that could damage the blood cells. Consequently, the efficiency of the valve would be reduced. Following the interpretation in Sect. 3.4.1, the delay of the left leaflet in the closing cycle could provide sufficient time to enable the retrograde flow to fully develop. This fully developed flow generates a stronger shear stress than the flow on the right. Indeed, the retrograde flow on the right produces a much smaller shear stress due to the shorter closing time of the right leaflet. It should also be emphasized that the limitations of the experimental setups could intensify the inverse flow. The absence of impedance in the systemic circulation could be ascribed to this intensified inverse flow.

4 Limitations

Several limitations of the current study should be noted. First, the experimental setups still need to be improved to mimic the physiological flow more efficiently. The short and long axes of the ventricle model should be designed for better similarity with the physiological state. Moreover, the impedance of the systemic circulation would also need to be added to the experimental setup to improve the simulation of the physiological state. Second, the VDV results indicate the three-dimensional nature of the ventricle flow. Even though this shows the advantage of VDV, it reflects

the shortcomings of the in-plane PIV measurement. Follow-up three-dimensional measurements would need to be conducted.

5 Conclusions

This paper presents an investigation of the full flow field of the left ventricle model with a SJM BMHV on the mitral position and a tilting-disk valve on the aortic position by utilizing PIV. Three typical physical flow phenomena were discussed by combining analyses conducted with different post-processing tools:

1. The triple jet pattern associated with SJM BMHV contains two strong lateral jets and one weak middle jet. Both the interaction among the three jets and the confines of the ventricle wall contribute to the phenomenon wherein only two clockwise vortices originate from the three jets. Adequate space next to the wall could be a necessary condition for the formation of the counter-clockwise vortex on the right side of the incoming jet. In addition, the two clockwise vortices have similar trajectories along the right wall of the ventricle model. The right vortex originating from the right lateral jet could also impede the emergence of the middle jet and contribute to a weak middle jet. Monitoring of the shear stress reveals that the triple jet pattern could introduce high shear stress within the ventricular flow, which should be avoided when prosthetic heart valves are implemented.
2. The effects of the two clockwise vortices on blood transportation are revealed using a combined analysis including LCSs tracking, shear stress monitoring, and the visualization of blood mixing by VDV. It is found that the utilization of the SJM BMHV complicates the ventricular flow and could reduce the efficiency of blood transportation. The left vortex could adversely affect the blood cells because of repeated damage resulting from shear stress.
3. The inverse flow near the SJM BMHV could result in asymmetric kinematics of the SJM BMHV leaflets. The asymmetric kinematics could also influence the triple jet pattern and the inverse flow.

Therefore, it is shown that the utilization of the SJM BMHV complicates the ventricular flow and changes the vortex dynamics within the ventricle completely. These effects could reduce the efficiency of blood transportation and result in complications.

Acknowledgements This work is supported by the National Natural Science Foundation of China (11472030, 11327202, and 11490552)

and the Fundamental Research Funds for Central Universities (YWF-16-JCTD-A-05).

References

- Akutsu T, Saito J (2006) Dynamic particle image velocimetry flow analysis of the flow field immediately downstream of bileaflet mechanical mitral prostheses. *J Artif Organs* 9(3):165–178
- Badas MG, Espa S, Fortini S, Querzoli G (2015) 3D finite-time Lyapunov exponents in a left ventricle laboratory model. In: EPJ Web of Conferences, EDP Sciences, vol 92
- Bermejo J, Martinez-Legazpi P, del Alamo JC (2015) The clinical assessment of intraventricular flows. *Annu Rev Fluid Mech* 47:315–342
- Carlier J, Stanislas M (2005) Experimental study of eddy structures in a turbulent boundary layer using particle image velocimetry. *J Fluid Mech* 535:143–188
- Cenedese A, Del Prete Z, Miozzi M, Querzoli G (2005) A laboratory investigation of the flow in the left ventricle of a human heart with prosthetic, tilting-disk valves. *Exp Fluids* 39(2):322–335
- Choi YJ, Vedula V, Mittal R (2014) Computational study of the dynamics of a bileaflet mechanical heart valve in the mitral position. *Ann Biomed Eng* 42(8):1668–1680
- Dasi LP, Ge L, Simon HA, Sotiropoulos F, Yoganathan AP (2007) Vorticity dynamics of a bileaflet mechanical heart valve in an axisymmetric aorta. *Phys Fluids* 19:067105 (1994-present)
- Dasi LP, Simon HA, Sucusky P, Yoganathan AP (2009) Fluid mechanics of artificial heart valves. *Clin Exp Pharmacol Physiol* 36(2):225–237 (19220329[pmid] Clin Exp Pharmacol Physiol)
- Eriksson J, Dyverfeldt P, Engvall J, Bolger AF, Ebberts T, Carlhall CJ (2011) Quantification of presystolic blood flow organization and energetics in the human left ventricle. *Am J Physiol Heart Circ Physiol* 300(6):H2135–H2141
- Eriksson J, Bolger AF, Ebberts T, Carlhall CJ (2012) Four-dimensional blood flow-specific markers of lv dysfunction in dilated cardiomyopathy. *Eur Heart J Cardiovasc Imaging* 13:159
- Espa S, Badas M, Fortini S, Querzoli G, Cenedese A (2012) A Lagrangian investigation of the flow inside the left ventricle. *Eur J Mech B/Fluids* 35:9–19
- Fallon AM, Marzec UM, Hanson SR, Yoganathan AP (2007) Thrombin formation in vitro in response to shear-induced activation of platelets. *Thromb Res* 121(3):397–406
- Faludi R, Szulik M, D'Hooge J, Herijgers P, Rademakers F, Pedrizzetti G, Voigt JU (2010) Left ventricular flow patterns in healthy subjects and patients with prosthetic mitral valves: an in vivo study using echocardiographic particle image velocimetry. *J Thorac and Cardiovasc Surg* 139(6):1501–1510
- Fortini S, Querzoli G, Cenedese A, Marchetti M (2008) The effect of mitral valve on left ventricular flow. Book *The Effect of Mitral Valve on Left Ventricular Flow*
- Fortini S, Querzoli G, Espa S, Cenedese A (2013) Three-dimensional structure of the flow inside the left ventricle of the human heart. *Exp Fluids* 54:1–9
- Fortini S, Querzoli G, Espa S, Cenedese A (2014) Three-dimensional structure of the flow inside the left ventricle of the human heart. arXiv preprint [arXiv:14077473](https://arxiv.org/abs/14077473)
- Gao Q, Wang H, Wang J (2012) A single camera volumetric particle image velocimetry and its application. *Sci China Technol Sci* 55(9):2501–2510
- Garitey V, Gandelheid T, Fuseri J, Pelissier R, Rieu R (1995) Ventricular flow dynamic past bileaflet prosthetic heart valves. *Int J Artif Organs* 18(7):380–391
- Gott VL, Alejo DE, Cameron DE (2003) Mechanical heart valves: 50 years of evolution. *Ann Thorac Surg* 76(6):S2230–S2239
- Grigioni M, Daniele C, D'Avenio G, Barbaro V (2002) Evaluation of the surface-averaged load exerted on a blood element by the Reynolds shear stress field provided by artificial cardiovascular devices. *J Biomech* 35(12):1613–1622
- Grigioni M, Daniele C, Morbiducci U, D'Avenio G, Di Benedetto G, Barbaro V (2004) The power-law mathematical model for blood damage prediction: Analytical developments and physical inconsistencies. *Artif Organs* 28(5):467–475
- He GS, Li N, Wang JJ (2014) Drag reduction of square cylinders with cut-corners at the front edges. *Exp Fluids* 55(6):1–11
- He GS, Wang JJ, Pan C, Feng LH, Gao Q, Rinoshika A (2017) Vortex dynamics for flow over a circular cylinder in proximity to a wall. *J Fluid Mech* 812:698–720
- Hendabadi S, Bermejo J, Benito Y, Yotti R, Fernández-Avilés F, del Álamo JC, Shadden SC (2013) Topology of blood transport in the human left ventricle by novel processing of doppler echocardiography. *Ann Biomed Eng* 41:2603–2616
- Kaminsky R, Kallweit S, Rossi M, Morbiducci U, Scalise L, Verdonck P, Tomasini E (2008) PIV measurements of flows in artificial heart valves, topics in applied physics. Springer, Berlin Heidelberg, pp 55–72
- Kheradvar A, Falahatpisheh A (2012) The effects of dynamic saddle annulus and leaflet length on transmitral flow pattern and leaflet stress of a bileaflet bioprosthetic mitral valve. *J Heart Valve Dis* 21(2):225
- Kheradvar A, Gharib M (2009) On mitral valve dynamics and its connection to early diastolic flow. *Ann Biomed Eng* 37(1):1–13
- Kheradvar A, Houle H, Pedrizzetti G, Tonti G, Belcik T, Ashraf M, Lindner JR, Gharib M, Sahn D (2010) Echocardiographic particle image velocimetry: a novel technique for quantification of left ventricular blood vorticity pattern. *J Am Soc Echocardiogr* 23(1):86–94
- Le TB, Sotiropoulos F (2013) Fluid-structure interaction of an aortic heart valve prosthesis driven by an animated anatomic left ventricle. *J Comput Phys* 244:41–62
- Okafor IU, Santhanakrishnan A, Chaffins BD, Mirabella L, Oshinski JN, Yoganathan AP (2015) Cardiovascular magnetic resonance compatible physical model of the left ventricle for multi-modality characterization of wall motion and hemodynamics. *J Cardiovasc Magn Reson* 17(1):1
- Pan C, Wang H, Wang J (2013) Phase identification of quasi-periodic flow measured by particle image velocimetry with a low sampling rate. *Meas Sci Technol* 24(5):055 305
- Pedrizzetti G, Domenichini F (2015) Left ventricular fluid mechanics: the long way from theoretical models to clinical applications. *Ann Biomed Eng* 43(1):26–40
- Pedrizzetti G, Domenichini F, Tonti G (2010) On the left ventricular vortex reversal after mitral valve replacement. *Ann Biomed Eng* 38(3):769–773
- Pibarot P, Dumesnil JG (2009) Prosthetic heart valves selection of the optimal prosthesis and long-term management. *Circulation* 119:1034–1048
- Pierrakos O, Vlachos PP (2006) The effect of vortex formation on left ventricular filling and mitral valve efficiency. *J Biomech Eng* 128(4):527–539
- Pierrakos O, Vlachos PP, Telonis DP (2004) Time-resolved DPIV analysis of vortex dynamics in a left ventricular model through bileaflet mechanical and porcine heart valve prostheses. *J Biomech Eng* 126(6):714–726
- Querzoli G, Fortini S, Cenedese A (2010) Effect of the prosthetic mitral valve on vortex dynamics and turbulence of the left ventricular flow. *Phys Fluids* 22(4):041901 (1994-present)
- Scarano F (2002) Iterative image deformation methods in PIV. *Meas Sci Technol* 13:R1
- Shadden SC, Taylor CA (2008) Characterization of coherent structures in the cardiovascular system. *Ann Biomed Eng* 36(7):1152–1162

- Shadden SC, Lekien F, Marsden JE (2005) Definition and properties of Lagrangian coherent structures from finite-time Lyapunov exponents in two-dimensional aperiodic flows. *Phys D Nonlinear Phenom* 212(3C4):271–304
- Shadden SC, Dabiri JO, Marsden JE (2006) Lagrangian analysis of fluid transport in empirical vortex ring flows. *Phys Fluids* 18(4):047105 (1994–present)
- Shadden SC, Astorino M, Gerbeau JF (2010) Computational analysis of an aortic valve jet with Lagrangian coherent structures. *Chaos Interdiscip J Nonlinear Sci* 20(1):017,512
- Son JW, Park WJ, Choi JH, Houle H, Vannan MA, Hong GR, Chung N (2012) Abnormal left ventricular vortex flow patterns in association with left ventricular apical thrombus formation in patients with anterior myocardial infarction. *Circ J* 76(11):2640–2646
- Sotiropoulos F, Le TB, Gilmanov A (2016) Fluid mechanics of heart valves and their replacements. *Ann Rev Fluid Mech* 48:259–283
- Tan SGD, Kim S, Hon JKF, Leo HL (2016) A D-shaped bileaflet bio-prosthesis which replicates physiological left ventricular flow patterns. *PLoS One* 11(6):e0156,580
- Toger J, Kanski M, Carlsson M, Kovacs SJ, Soderlind G, Arheden H, Heiberg E (2012) Vortex ring formation in the left ventricle of the heart: analysis by 4D flow MRI and Lagrangian coherent structures. *Ann Biomed Eng* 40(12):2652–2662
- Wang H, Gao Q, Feng L, Wei R, Wang J (2015) Proper orthogonal decomposition based outlier correction for PIV data. *Exp Fluids* 56(2):1–15
- Wang J, Pan C, Choi KS, Gao L, Lian QX (2013) Formation, growth and instability of vortex pairs in an axisymmetric stagnation flow. *J Fluid Mech* 725:681–708
- Yoganathan AP, He Z, Casey Jones S (2004) Fluid mechanics of heart valves. *Annu Rev Biomed Eng* 6:331–362
- Yun BM, Dasi L, Aidun C, Yoganathan A (2014a) Highly resolved pulsatile flows through prosthetic heart valves using the entropic lattice-boltzmann method. *J Fluid Mech* 754:122–160
- Yun BM, McElhinney DB, Arjunon S, Mirabella L, Aidun CK, Yoganathan AP (2014b) Computational simulations of flow dynamics and blood damage through a bileaflet mechanical heart valve scaled to pediatric size and flow. *J Biomech* 47(12):3169–3177. doi:10.1016/j.jbiomech.2014.06.018
- Zhou J, Adrian RJ, Balachandar S, Kendall T (1999) Mechanisms for generating coherent packets of hairpin vortices in channel flow. *J Fluid Mech* 387:353–396